NORTHWESTERN UNIVERSITY

Operando studies of atomic layer deposition of dielectrics on transition metal dichalcogenide transistors

A Thesis
Submitted to the Department of Materials Science and Engineering
In partial fulfillment of the requirements for the degree

Master of Science

Field of Materials Science and Engineering

By
Ju Ying Shang

December 16, 2019

Table of Contents

Abstract

Layered transition metal dichalcogenides (TMDs) and two-dimensional (2D) materials are widely studied as complements to Si complementary metal-oxide-semiconductor technology. Field-effect transistors (FETs) made with 2D materials often exhibit mobilities below their theoretical limit. Encapsulation with dielectrics grown by atomic layer deposition (ALD) can be used to tune carrier concentrations and improve mobility. While molecular adsorbates are known to dope 2D materials and influence charge scattering mechanisms, it is not well understood how ALD reactants affect 2D transistors during growth. We demonstrate exposures to ambient oxidants, H_2O and O_2, induce reversible electronic changes on $MoTe_2$ FETs, indicating negligible oxidation takes place during exposure. During ALD growths with H_2O as the oxidant, oxidation reactions do not have to be considered for TMDs as stable as $MoTe_2$. More importantly, we report *operando* electronic measurements on MoS_2 and $MoTe_2$ FETs during ALD MoO_x growth, which reveal mobility improvement at the first cycle. Real-time monitoring of current density during ALD growth was used to correlate a decrease in the potential perturbation and density of charged scattering centers with the first metal-organic pulse. Additionally, mobility analysis with variable temperature measurements confirmed that there is a reduction in charged impurity scattering.

Introduction

Controlling carrier concentration and improving mobility are key elements of complementary metal-oxide-semiconductor (CMOS) technology. However, CMOS scaling is approaching fundamental limits[1], indicating new materials and technologies are needed. Layered transition metal dichalcogenides (TMDs) and other two-dimensional (2D) materials are promising candidates for complementing CMOS[2]. Transistors are the building blocks of CMOS technology. An optimized field-effect transistor (FET) has a highest-possible mobility such that it can be quickly switched on and off and a carrier concentration that can be tuned to meet its application requirements. Transistors made with 2D materials often demonstrate mobilities below their theoretical limit[3]. Therefore, it is necessary to control carrier concentration and improve mobility of 2D materials. Here, we focus on MoS_2 and $MoTe_2$. MoS_2 is an ambient-stable TMD that is heavily studied. $MoTe_2$ is unstable in ambient[4], but it has interesting properties, such as being ambipolar with a bandgap similar to Si[5] and exhibiting a low energy barrier for semiconductor-to-metal transition[6]. These properties allow for novel device structures[7,8].

Many processes dope TMDs, but not all of them improve mobility. Substitutional doping tends to degrade mobility due to generation of defects that scatter carriers[9]. Charge transfer doping with molecular adsorbates or metal nanoparticles can increase mobility[10], but this doping scheme generally requires additional processing to ensure long-term stability. Charge transfer doping with dielectric encapsulation has the potential to improve mobility[11] and promote ambient stability[12] at the same time. In previous work, MoO_x, grown with atomic layer deposition (ALD), was used to dope MoS_2 with electrons or holes[13]. ALD-grown dielectric encapsulation is desirable because it can be performed at temperatures compatible with polymeric materials and can be used on large area substrates[14].

Doping TMDs with dielectric encapsulation is generally attributed to transferring of charges due to differences in energy level alignment[9,11]. Other reports have also claimed diffusion of ions[15] or fixed charges[16] to explain modulation of carrier concentration for TMDs with ALD encapsulation. Insight into processes that influence carrier concentration during ALD encapsulation of TMDs is essential for understanding doping of TMDs. Currently, evidence in this area is lacking.

Mobility has been shown to improve significantly with ALD oxide encapsulation[17]. With encapsulation, two scattering sources are impacted[3] – remote phonons are introduced from the encapsulation and charged impurity (CI) scattering is affected. Remote phonons scatter carriers, and therefore degrade mobility. However, remote and intrinsic phonons play a secondary role in charge transport for TMDs, compared to CIs[18]. Conventionally, charged scattering centers of any type, such as impurities, adsorbates, interface traps, etc., are collectively referred to as charged impurities. In general, improving mobility with dielectric encapsulation is attributed to dielectric screening[3,19], which reduces the Coulomb potential of all CIs.

However, dielectric screening is not the only way to reduce CI scattering. The density of CIs, or more precisely, the density of large variations in the Coulomb potential of the TMD can be reduced as well[20], smoothing out the charge distribution. Previously employed methods, such as a growth series with varying dielectric thickness[21,22], are not able to identify when a reduction in density of CIs has occurred. A growth series with varying dielectric thickness can provide information on the evolution of changes in mobility and doping, allowing for investigation into how the evolution happens[21]. However, prior to full dielectric coverage, ambient contamination will make interpretation of results from *ex situ* growth series difficult.

Operando monitoring of electronic changes during ALD growth on TMDs has enabled us to address key questions. Oxidants have been shown to oxidize the surface of TMDs[23-25], changing the electronic band structure at the same time[26]. ALD reactions involve oxidants. This brings up the question of how oxidants affect electronic properties before ALD film coverage is complete, especially for unstable TMDs, such as $MoTe_2$. In addition, as noted previously, exposure to gaseous molecules dope TMDs as well[10]. Prior to complete oxide film coverage, TMDs are exposed to alternating pulses of metal organics and oxidants. Both reactants will induce changes in mobility and carrier concentration[27]. This raises the question of how initial cycles of the ALD growth change the charge distribution at the TMD-encapsulation interface, ultimately influencing device properties. The progression of changes in electronic properties with increasing dielectric thickness can provide valuable information for how doping and mobility evolve[28].

Here we report *operando* electronic measurements on MoS_2 and $MoTe_2$ FETs during ALD MoO_x growth. Ambient oxidants, H_2O and O_2, have been claimed to dope these two TMDs[29,30]. We have confirmed these claims for $MoTe_2$ and demonstrated that they induce reversible electronic changes, suggesting that negligible oxidation takes place during short exposures between 80 and 180 °C. As such, during ALD MoO_x growth at 80 °C with H_2O as the oxidant, oxidation reactions do not have to be considered. With *operando* analysis during ALD growth, this thesis shows that the initial cycles disproportionately affect final device properties. After the first five growth cycles, for MoS_2, carrier concentration increased by 60 % and mobility increased by 160 %. For $MoTe_2$, carrier concentration increased by 50 % and mobility increased by 840 %. We attribute the increase in mobility to reductions in the potential perturbation and density of CIs. Mobility analysis with variable temperature measurements confirmed the reduction in CI scattering.

Results and Discussion

Figure 1a shows an optical micrograph of a typical $MoTe_2$ FET. $MoTe_2$ crystals were grown using chemical vapor transport at NIST in Gaithersburg. MoS_2 crystals were purchased from SPI Supplies. To fabricate

FETs, $MoTe_2$ and MoS_2 crystals were mechanically exfoliated onto 285 nm SiO_2/Si wafers, with degenerately doped Si as the back gate. A standard two-step electron-beam lithography process was used to define contacts, which were thermally evaporated gold. For *operando* experiments, MoS_2 and $MoTe_2$ FETs were connected to three terminals (**Figure 1b**) and loaded into the modified ALD chamber (**Figure 1c**). During metal organic and oxidant pulses, electronic responses were recorded. After every five cycles of growth, a transfer curve was measured. Amorphous MoO_x was grown at 80 °C with $Mo(NMe_2)_4$ and H_2O as the reactants. MoO_x stoichiometry was close to MoO_2[13]. For ambient stability, Al_2O_3 with trimethylaluminum (Sigma) and H_2O was grown after MoO_x growth.

Oxidant Exposures

Here, we start with oxidant exposures on $MoTe_2$. Real-time monitoring of electronic changes during exposure to O_2 and H_2O confirms that these two oxidants make the n-type channel less conductive (**Figures 1d, e, h, i**). The measured current is proportional to the conductivity $\sigma = ne\mu_e + pe\mu_h$. The figures show the sheet current density I_{DS} or current per unit width to enable comparison between devices The decrease in current density shown in **Figure 1d and 1e** is caused by a decrease in electron concentration and/or mobility (**Figures 1h and 1i** shows the transfer characteristics). The change in electron mobility is negligible for $MoTe_2$ exposed to O_2 (25 to 24 $cm^2/V{\cdot}s$) and for $MoTe_2$ exposed to H_2O (25 to 26 $cm^2/V{\cdot}s$). Thus, the decrease in current density with oxygen and water exposure is mostly due to a decrease in electron concentration, likely due to oxygen molecules or water adsorbed on the surface acting as an acceptor[16,29].

Reference [16] showed that annealing between 4 and 40 mTorr increases hole conductivity and decreases electron conductivity for $MoTe_2$ FETs. Reference [29] demonstrated that exposure to air at room temperature results in similar changes in $MoTe_2$ carrier conductivity. Both references cited DFT calculations[26] postulating oxygen atoms are substituted into $MoTe_2$ lattice via adsorption-mediated dissociation, causing an increase in hole concentration. However, neither reference included a discussion of changes in mobility showing the effects of air exposure. Our observations in **Figures 1d, e, h, i** reveal O_2 and H_2O exposure changes mobility minimally, confirming that these two oxidants dope $MoTe_2$, as claimed by references [16,29]. In addition, we have observed the changes in electronic properties when exposed to oxygen and water can be reversed with annealing (**Figures 1h and 1i**), indicating, at the ALD growth temperature (80 to 180 °C) and the timescale for exposure to ALD reactants (30 min or less), the two oxidants do not react irreversibly with $MoTe_2$.

Operando measurements during exposure to O_3 (**Figures 1f, g, j**) confirm that O_3 hole-dopes $MoTe_2$ irreversibly. Post ozone exposure, electron mobility decreases by two orders of magnitude (19 to 0.2 $cm^2/V{\cdot}s$). In **Figure 1f**, the current density decreases with the first three pulses, and in **Figure 1g** it increases with the subsequent three pulses, which directly followed the first three pulses in **Figure 1f**. This

observation reveals O_3 can induce irreversible changes in carrier concentration and mobility (confirmed in **Figure 1j**), as opposed to O_2 and H_2O, which induced reversible changes. The irreversibility is likely due to oxidation of $MoTe_2$ surface[23].

Operando ALD

Given H_2O exposures between 80 and 180 °C do not induce irreversible changes in mobility and carrier concentration, oxidation during ALD growths with H_2O can be ruled out. However, as noted in the Introduction, exposure to ALD reactants will induce changes in electronic properties on TMDs. The question still remains: what happens to TMDs during the initial cycles of ALD growth? To answer this question, we conducted *operando* measurements on MoS_2 (**Figure 2**) and $MoTe_2$ (**Figure 3**) FETs during an ALD MoO_x growth, with alternating pulses of $Mo(NMe_2)_4$ and H_2O. $Mo(NMe_2)_4$ was synthesized according to a method described in references [31,32] by members of Tobin Marks' group. The ALD reactor was a modified Ultratech Savannah S200 with *in situ* quartz crystal microbalance (QCM) and insulated lid. The two-step cycle consisted of $Mo(NMe_2)_4$ dose, 30 s purge, H_2O dose, and 30 s purge. Following MoO_x growth, Al_2O_3 was grown. All MoO_x and Al_2O_3 films were ca. 10 nm thick and grown at 80 °C. *Operando* measurements were conducted as follows. One transfer curve measurement (V_{DS} set at 0.5 V) was taken after every five ALD growth cycles. During each ALD cycle, V_G was set at 55 V to bring the FETs into strong accumulation such that the measured I_{DS} (with V_{DS} set at 0.05 V) had a high signal-to-noise ratio.

Figure 2a shows real-time monitoring of current density I_{DS} of MoS_2 during the first five cycles of MoO_x growth. The inset shows current density during the entire ALD growth. **Figure 2b** shows consecutive transfer curves collected every five ALD cycles, for the first 35 cycles. **Figure 2c** shows transport characteristics for the rest of the growth, during which I_{DS} decreases. From each transfer curve, carrier concentration n_{2D} (**Figure 2d**) and intrinsic mobility μ_0 (**Figure 2e**) were extracted using the Y-function method (see Methods for details). Our *operando* charge transport analysis reveals a sharp increase in carrier concentration and mobility at the beginning of ALD MoO_x growth. After the first five cycles, for MoS_2, n_{2D} increased by 60 % and μ_0 increased by 160 %. I_{DS} increased by 140 % at the end of the first cycle.

The electron conductivity is $\sigma_n = ne\mu_n$, which is proportional to I_{DS}. An increase in σ_n or I_{DS} indicates an increase in n, μ_n, or both. Our observations show that five ALD cycles increase both n_{2D} and μ_0 for MoS_2. To calculate an upper and lower bound for percent increase in mobility at the end of the first cycle, one can assume a monotonic increase in n_{2D}. **Appendix Table 1** records all values used for the calculations. For MoS_2, after the first cycle of growth, mobility increases between 50 to 140 %.

A $MoTe_2$ FET was loaded with the MoS_2 FET during the same MoO_x growth. **Figure 3a** shows $MoTe_2$ current density I_{DS} during the first five cycles of MoO_x growth, with the inset showing I_{DS} during the entire growth. **Figure 3b** shows consecutive transfer curves collected every five ALD cycles for the

entire MoO_x growth, and **Figure 3c** shows the same characteristic curves on a log scale. Using the Y-function method, we extracted n_{2D} (**Figure 3d**) and μ_0 (**Figure 3e**). Similar to MoS_2, after the first five ALD growth cycles, there is a sharp increase in n_{2D} (by 50 %) and μ_0 (by 840 %) for $MoTe_2$. Likewise, I_{DS} increased by 2100 % at the end of the first ALD cycle. Using the same assumption, we estimate mobility to increase between 340 to 2100 % after the first cycle of growth. **Appendix Table 2** records all values used for percent increase calculations for $MoTe_2$.

An increase in mobility signifies carrier scattering has reduced. According to Yu *et al.*[3], sources of scattering in 2D FETs are 1) intrinsic electron-phonon scattering, 2) polar surface optical phonon scattering, 3) charged impurity (CI) scattering, and 4) atomic defect scattering, specifically referring to scattering from uncharged intrinsic defects. The intrinsic phonon-limited mobility is the highest-possible mobility, but it can only be achieved in samples free of other scattering sources. In practice, however, 2D FETs cannot be free of impurities or defects and need to be supported by a substrate. Polar surface optical phonons are remote phonons from the substrate or the encapsulation that cause inelastic carrier scattering. Near room temperature, remote phonons can become the dominant scattering mechanism[33], implying that encapsulation may degrade mobility in pristine samples. For both MoS_2 and $MoTe_2$, we have observed an overall increase in mobility with MoO_x encapsulation, indicating that remote phonons do not dominate scattering here. Scattering from atomic defects is short-range and independent of temperature or carrier density[3]. This background scattering due to intrinsic defects in 2D materials is secondary compared to scattering from CIs. Thus, in this thesis, we focus on CI scattering, as it is the dominant mechanism limiting mobility, overshadowing contributions from other sources[3,18]. It is important to note that CIs are not exclusively impurities; CIs are large localized variations in the potential energy surface of the semiconductor due to impurities, adsorbates, or interface traps.

Encapsulation with a dielectric prompts consideration of dielectric screening as a mechanism for improving mobility. However, with the first cycle of growth, the final MoO_x dielectric has not yet covered the surface. Instead, we must consider changes induced by a single pulse, including interactions between individual reactant molecules and the TMD surface. In **Figure 2a and Figure 3a,** the initial increase in I_{DS} corresponds to the first metal-organic pulse. The subsequent decrease in I_{DS} corresponds to the first H_2O pulse. **Appendix Figure 1** correlates changes in chamber pressure with current density responses. *In situ* QCM monitoring reveals that during H_2O pulses, there is a sharp increase in thickness followed by a decay (**Appendix Figure 2**). This transient response indicates an exothermic reaction has taken place[34]. While the current density response to the H_2O pulse is due to a chemical reaction, the large increase in I_{DS} due to the first metal-organic pulse is not induced by an irreversible chemical reaction between the metal-organic and the TMD lattice. In our prior work[13], we have confirmed ALD MoO_x growth with H_2O nucleates without covalent bonding to the underlying MoS_2.

Based on the discussion above, we conclude that metal-organic molecules interact with CIs on the TMD surface by neutralizing, displacing, or screening them[35,36]. All of these interactions decrease the magnitude of the potential variations and may reduce the density of CIs.

Operando ALD with Masked FETs

Molecular adsorption and oxide growth at the near-contact region can affect transport properties[37]. To examine if the mobility increase noted previously is due to modulation at the contacts, we fabricated masked FETs with MoS_2. Electron-beam lithography was used to define the masked region and ALD-grown Al_2O_3 with thickness of 10 nm was the mask material. Prior to *operando* MoO_x growth, transport characteristics of the masked FETs were showing typical MoS_2 FET behavior, ensuring the masked FETs are comparable to the unmasked ones. **Figure 4a** shows a schematic of masked MoS_2 FET where the contacts are masked and the channel is exposed (Exposed Channel), and **Figure 4b** shows a schematic of a masked MoS_2 FET where the channel is masked and the contacts are exposed (Exposed Contacts). **Appendix Figures 3a and 3e** show AFM scans of the Exposed Channel and Exposed Contacts FETs, respectively. The same *operando* measurement parameters were used for masked FETs during a second MoO_x growth with the same two-step cycle and growth temperature.

With the Exposed Channel FET, we can isolate how the channel is being modulated during ALD growth. **Figure 4c** shows a negligible change in carrier concentration after the first five ALD cycles, and **Figure 4d** shows a 50 % increase in mobility. After the first cycle, **Appendix Figure 3b** shows a 40 % increase in current density. **Appendix Table 3** records all the values used for percent increase calculations. With the contacts masked, any change in the FET originates from changes to the channel. The increases in mobility and current density for the Exposed Channel FET provide evidence that the first ALD cycle reduces the potential perturbation and density of the CIs, rather than modulating properties at the contacts.

Operando measurements with the Exposed Contacts FET do not allow as direct an interpretation as did the Exposed Channel FET. Due to fabrication limitations, a small portion of the channel is exposed in the Exposed Contacts FET. Any changes in carrier concentration and mobility originate from changes at the near-contact region and the nearby channel region. **Figure 4e** shows a 30 % increase in carrier concentration after the first five ALD cycles, and **Figure 4f** shows a 10 % increase in mobility. After the first cycle, **Appendix Figure 3f** shows a 40 % increase in current density. **Appendix Table 4** records all the values used for percent increase calculations. While it is not possible to attribute the increases solely to modulation at the near-contact region, these increases demonstrate the FET is not operating in the contact-limited transport regime. If contacts were limiting charge injection into the channel, one would expect to see comparable changes in n_{2D}, μ_0, and I_{DS} as those observed with the unmasked MoS_2 FET (shown in

Figure 2 and **Appendix Table 1**). Given the same fabrication procedure is utilized, this conclusion can be extended to all FETs in this thesis.

Thus far, we have focused on mobility at the beginning of MoO_x growth. There is another notable trend in mobility trends upon ~ 3 nm of nominal oxide growth, where, in **Figures 4d and 4f**, mobility starts to decrease. **Figure 2e** for MoS_2 and **Figure 3e** for $MoTe_2$ exhibit the same feature. One explanation for the decrease in mobility starting at ~ 3 nm of nominal oxide thickness is that the dielectric stoichiometry is still evolving, changing the fixed charge in the dielectric. The Coulomb potential variations arising from the fixed charge scatter carriers, decreasing mobility. Prior to 3 nm, the decrease in scattering due to reduction in the potential variations and density of CIs outweighed the increase in scattering due to fixed charge, resulting in an overall increase in mobility. This imbalance is especially pronounced at the first ALD cycle.

Variation of Mobility with Temperature

Below, we analyze how mobility varies with temperature by fitting to the expression $\mu \sim T^{-\gamma}$, where a change in γ indicates a change in the dominant source of scattering. In the CI-dominated transport regime, a decrease in γ indicates a reduction in CI scattering. **Figure 5** shows γ decreased from 2.5 to 0.28 with MoO_x encapsulation for $MoTe_2$. For MoS_2, γ is expected to decrease with encapsulation as well.

Reference [17] has observed a reduction in γ for MoS_2 when encapsulated with ALD-grown HfO_2, consistent with **Figure 5**. The reduction in γ was compared to theoretically-predicted values in the phonon-limited transport regime. The results could also be explained by a reduction in density of CIs, which was not discussed. Reference [38] has shown that when encapsulated with h-BN, there is an increase in γ for MoS_2 FETs. The increase in γ could be due to a change in the dominant source of scattering from CI to phonon. Or it could be due to an increase in density of CIs, potentially originating from polymer residue and trapped hydrocarbons during h-BN transfer. Regardless, the overall mobility still increased with h-BN encapsulation, indicating the effect of the increase in density of CIs and/or the switch from CI to phonon-dominated scattering was mitigated by the increased dielectric screening.

For $MoTe_2$, there is one report with mobility analysis from variable temperature measurements[15], which showed temperature-mobility trends that differ from those shown in **Figure 5**. In this report, the authors observed that mobility increased with increasing temperature for unencapsulated $MoTe_2$ FETs. When encapsulated with ALD-grown Al_2O_3, mobility decreased with increasing temperature. The claim is that with encapsulation, charge transport switched from hopping to band-like. In **Figure 5**, prior to encapsulation, mobility decreases with increasing temperature in the 180-353 K range. With MoO_x encapsulation, the trend did not change, but γ decreased. The discrepancy with Ref. [15] could be due to

differences in FET thickness and/or differences in fabrication technique resulting in different contact properties. The authors are using $MoTe_2$ FETs that are five layers or thinner. Charge transport for FETs with five layers or less is dominated by impurities at the gate oxide-semiconductor interface[39], which may result in hopping transport. In addition, the contacts from reference [15] were sputtered. Reactions at the contacts can result in contact-limited transport processes[40], resulting in different mobility trends.

Conclusion

With *operando* experiments, we have demonstrated the significant impact of the initial ALD cycle on final device properties. Carrier concentration and mobility both increase within the first five ALD cycles. We attribute the increase in mobility to a reduction in potential perturbation and density of charged scattering centers due to interactions between ALD reactants and impurities, adsorbates, interface traps on the TMD surface.

Given how sensitive device properties are to the initial ALD cycle, the condition of the device surface needs to be considered, especially since there are variations in ambient conditions. If the device has been exposed to ambient, surface cleaning should be conducted prior to dielectric deposition for reproducibility. Seeding layers have also been used to promote ALD growths[41]. In addition to choosing a seeding layer that facilitates nucleation, it is necessary to consider how the seeding layer will influence the TMD-encapsulation interface and interact with the charge distribution of the TMD. A common seeding choice is strong oxidants, such as ozone, which will oxidize TMD surface[23,42,43]. In ALD processes with ozone or other reactive chemicals, the relationship between surface chemistry and electronic properties of the device should be established.

Methods

Y-function Extraction of V_{Th} and μ_0

Source-drain current during strong accumulation (when the transconductance was decreasing) was modeled with Equation (1) below[44,45], which assumed constant contact resistance and variable channel resistance,

$$I_D = \frac{W}{L} C_{gate} (V_G - V_{Th}) \frac{\mu_0}{1+\theta \cdot (V_G - V_{Th})} \cdot V_D \quad (1)$$

where I_D was the source-drain current and V_D was the applied source-drain bias, W and L were the width and length of the FET channel, respectively. C_{gate} was the capacitance of the gate dielectric, V_G was the applied gate bias, V_{Th} was the threshold voltage, μ_0 was the intrinsic mobility of the channel, and θ was

the mobility attenuation factor, which could be expressed as $\theta = (W/L)\mu_0 C_{gate} R_{contacts}$, where $R_{contacts}$ was the contact resistance.

To extract V_{Th} and μ_0, we assumed mobility to be carrier-concentration independent. In multilayer TMDs, carriers near the gate dielectric-TMD interface screen impurities at the interface, reducing scattering for carriers farther away from the interface[39]. Likewise, with multilayer TMDs, where carriers screened changes at the top ALD growth surface, gate capacitance could be assumed to be constant during oxide growth[38]. Using the parallel-plate approximation, the carrier concentration is $n_{2D} = C_{gate}(V_G - V_{Th})/e$, where e is the elementary charge.

During oxide growth, contact resistance changed minimally (**Appendix Figure 5a**). In order to fit source-drain current with less noise, contact resistance for each transfer curve was set as the average contact resistance of all the extracted $R_{Contact}$ from *operando* ALD growth. With variable temperature measurements (80 K to 353 K), mobility was extracted with constant contact resistance. Contact resistance varied within 1 kΩ (**Appendix Figure 5b**), which was on the same order of magnitude as errors associated with parameter extraction. To reduce fitting noise, contact resistance was set to be the average value of the extracted $R_{Contact}$ within the temperature range.

Percent Increase Calculations

Percent increase was calculated with the following formula,

$$\%\ Increase = \left(\frac{New\ Value}{Original\ Value} - 1\right) \times 100\%$$

To calculate the lower and upper bounds in mobility percent increase, the following calculation steps were performed,

$$n_0 \cdot e \cdot \mu_0 = \sigma_0$$

$$\left(\frac{n_1}{n_0}\right) \cdot n_0 \cdot e \cdot \left(\frac{\mu_1}{\mu_0}\right) \cdot \mu_0 = \left(\frac{\sigma_1}{\sigma_0}\right) \cdot \sigma_0$$

$$\left(\frac{n_1}{n_0}\right) \cdot \left(\frac{\mu_1}{\mu_0}\right) = \left(\frac{\sigma_1}{\sigma_0}\right)$$

$$\left(\frac{\mu_1}{\mu_0}\right) = \left(\frac{\sigma_1}{\sigma_0}\right) \Big/ \left(\frac{n_1}{n_0}\right)$$

where n_0, μ_0, σ_0 are the electron concentration, mobility, and conductivity, respectively, before ALD growth (ALD cycle 0), n_1, μ_1, σ_1 are the electron concentration, mobility, and conductivity, respectively, at the end of the first ALD cycle (ALD cycle 1). For calculating the lower and upper bounds, carrier concentration is assumed to monotonically increase from cycle 0 to cycle 5. For calculating the lower bound, σ_0 is the conductivity extracted from the transfer curve on the forward sweep. To calculate the upper bound, σ_0 is the conductivity extracted from the transfer curve on the backward sweep.

References

1 International Technology Roadmap for Semiconductors 2.0: Beyond CMOS. 1-87 (2015).

2 Akinwande, D. *et al.* Graphene and two-dimensional materials for silicon technology. *Nature* **573**, 507-518, doi:10.1038/s41586-019-1573-9 (2019).

3 Yu, Z. *et al.* Analyzing the Carrier Mobility in Transition-Metal Dichalcogenide MoS2 Field-Effect Transistors. *Advanced Functional Materials* **27**, doi:10.1002/adfm.201604093 (2017).

4 Chen, B. *et al.* Environmental Changes in MoTe2 Excitonic Dynamics by Defects-Activated Molecular Interaction. *ACS Nano* **9**, 5326-5332, doi:10.1021/acsnano.5b00985 (2015).

5 Ruppert, C., Aslan, O. B. & Heinz, T. F. Optical properties and band gap of single- and few-layer MoTe2 crystals. *Nano Lett* **14**, 6231-6236, doi:10.1021/nl502557g (2014).

6 Wang, Y. *et al.* Structural phase transition in monolayer MoTe2. *Nature* **550**, 487, doi:doi:10.1038/nature24043 (2017).

7 Hou, W. *et al.* Strain-based room-temperature non-volatile MoTe2 ferroelectric phase change transistor. *Nat Nanotechnol* **14**, 668-673, doi:10.1038/s41565-019-0466-2 (2019).

8 Cho, S. *et al.* Phase patterning for ohmic homojunction contact in MoTe2. *Science* **349**, 625-628, doi:10.1126/science.aab3175 (2015).

9 Luo, P. *et al.* Doping engineering and functionalization of two-dimensional metal chalcogenides. *Nanoscale Horizons* **4**, 26-51, doi:10.1039/c8nh00150b (2019).

10 Zhang, X., Shao, Z., Zhang, X., He, Y. & Jie, J. Surface Charge Transfer Doping of Low-Dimensional Nanostructures toward High-Performance Nanodevices. *Adv Mater* **28**, 10409-10442, doi:10.1002/adma.201601966 (2016).

11 Hu, Z. *et al.* Two-dimensional transition metal dichalcogenides: interface and defect engineering. *Chem Soc Rev* **47**, 3100-3128, doi:10.1039/c8cs00024g (2018).

12 Li, Q., Zhou, Q., Shi, L., Chen, Q. & Wang, J. Recent advances in oxidation and degradation mechanisms of ultrathin 2D materials under ambient conditions and their passivation strategies. *Journal of Materials Chemistry A* **7**, 4291-4312, doi:10.1039/c8ta10306b (2019).

13 Moody, M. J. *et al.* Atomic Layer Deposition of Molybdenum Oxides with Tunable Stoichiometry Enables Controllable Doping of MoS2. *Chemistry of Materials* **30**, 3628-3632, doi:10.1021/acs.chemmater.8b01171 (2018).

14 George, S. M. Atomic Layer Deposition: An Overview. doi:10.1021/cr900056b (2009).

15 Lee, H. S. *et al.* Impact of H-Doping on n-Type TMD Channels for Low-Temperature Band-Like Transport. *Small*, e1901793, doi:10.1002/smll.201901793 (2019).

16 Qu, D. *et al.* Carrier-Type Modulation and Mobility Improvement of Thin MoTe2. *Adv Mater* **29**, doi:10.1002/adma.201606433 (2017).

17 Radisavljevic, B. & Kis, A. Mobility engineering and a metal-insulator transition in monolayer MoS(2). *Nat Mater* **12**, 815-820, doi:10.1038/nmat3687 (2013).

18 Ma, N. & Jena, D. Charge Scattering and Mobility in Atomically Thin Semiconductors. *Physical Review X* **4**, doi:10.1103/PhysRevX.4.011043 (2014).

19 Ong, Z.-Y. & Fischetti, M. V. Mobility enhancement and temperature dependence in top-gated single-layer MoS2. *Physical Review B* **88**, doi:10.1103/PhysRevB.88.165316 (2013).

20 S. Li, K. T., E. Orgiu, P. Samori. Charge Transport and Mobility Engineering in Two-Dimensional Transition Metal Chalcogenide Semiconductors. *Chemical Society Reviews* **45**, 1-226, doi:10.1039/c5cs00517e (2015).

21 Luo, W. *et al.* Carrier Modulation of Ambipolar Few-Layer MoTe2 Transistors by MgO Surface Charge Transfer Doping. *Advanced Functional Materials*, doi:10.1002/adfm.201704539 (2017).

22 Xu, J. *et al.* Effects of HfO2 encapsulation on electrical performances of few-layered MoS2 transistor with ALD HfO2 as back-gate dielectric. *Nanotechnology* **29**, 345201, doi:10.1088/1361-6528/aac853 (2018).

23 Zheng, X. *et al.* Controlled Layer-by-Layer Oxidation of MoTe2 via O3 Exposure. *ACS Appl Mater Interfaces* **10**, 30045-30050, doi:10.1021/acsami.8b11003 (2018).

24 Seo, S.-Y. *et al.* Writing monolithic integrated circuits on a two-dimensional semiconductor with a scanning light probe. *Nature Electronics* **1**, 512-517, doi:10.1038/s41928-018-0129-6 (2018).

25 Peto, J. *et al.* Spontaneous doping of the basal plane of MoS2 single layers through oxygen substitution under ambient conditions. *Nat Chem*, doi:10.1038/s41557-018-0136-2 (2018).

26 Liu, H., Han, N. & Zhao, J. Atomistic insight into the oxidation of monolayer transition metal dichalcogenides: from structures to electronic properties. *RSC Advances* **5**, 17572-17581, doi:10.1039/c4ra17320a (2015).

27 Jandhyala, S. *et al.* Atomic Layer Deposition of Dielectrics on Graphene Using Reversibly Physisorbed Ozone. *ACS Nano* **6**, 2722-2730 (2012).

28 Qi, D. *et al.* Continuously Tuning Electronic Properties of Few-Layer Molybdenum Ditelluride with in Situ Aluminum Modification toward Ultrahigh Gain Complementary Inverters. *ACS Nano* **13**, 9464-9472, doi:10.1021/acsnano.9b04416 (2019).

29 Chang, Y. M. *et al.* Reversible and Precisely Controllable p/n-Type Doping of MoTe2 Transistors through Electrothermal Doping. *Adv Mater*, doi:10.1002/adma.201706995 (2018).

30 Schmidt, H. *et al.* Transport properties of monolayer MoS2 grown by chemical vapor deposition. *Nano Lett* **14**, 1909-1913, doi:10.1021/nl4046922 (2014).

31 Bradley, D. C. & Chisholm, M. H. Covalent compounds of quadrivalent transition metals. Part V. Molybdenum(IV) dialkylamides. *Journal of the Chemical Society A: Inorganic, Physical, Theoretical*, doi:10.1039/j19710002741 (1971).

32 Jurca, T. *et al.* Low-Temperature Atomic Layer Deposition of MoS2 Films. *Angew Chem Int Ed Engl* **56**, 4991-4995, doi:10.1002/anie.201611838 (2017).

33 Yu, Z. *et al.* Realization of Room-Temperature Phonon-Limited Carrier Transport in Monolayer MoS2 by Dielectric and Carrier Screening. *Adv Mater* **28**, 547-552, doi:10.1002/adma.201503033 (2016).

34 Christensen, S. T. & Elam, J. W. Atomic Layer Deposition of Ir−Pt Alloy Films. *Chemistry of Materials* **22**, 2517-2525, doi:10.1021/cm9031978 (2010).

35 Worley, B. C., Haws, R. T., Rossky, P. J. & Dodabalapur, A. Chemical Understanding of the Mechanisms Involved in Mitigation of Charged Impurity Effects by Polar Molecules on Graphene. *The Journal of Physical Chemistry C* **120**, 12909-12916, doi:10.1021/acs.jpcc.6b03853 (2016).

36 Worley, B. C. *et al.* Dramatic vapor-phase modulation of the characteristics of graphene field-effect transistors. *Phys Chem Chem Phys* **17**, 18426-18430, doi:10.1039/c5cp01888a (2015).

37 Duran Retamal, J. R., Periyanagounder, D., Ke, J. J., Tsai, M. L. & He, J. H. Charge carrier injection and transport engineering in two-dimensional transition metal dichalcogenides. *Chem Sci* **9**, 7727-7745, doi:10.1039/c8sc02609b (2018).

38 Liu, Y. *et al.* Toward barrier free contact to molybdenum disulfide using graphene electrodes. *Nano Lett* **15**, 3030-3034, doi:10.1021/nl504957p (2015).

39 Li, S. L. *et al.* Thickness-dependent interfacial Coulomb scattering in atomically thin field-effect transistors. *Nano Lett* **13**, 3546-3552, doi:10.1021/nl4010783 (2013).

40 Mleczko, M. J. *et al.* Contact Engineering High-Performance n-Type MoTe2 Transistors. *Nano Lett* **19**, 6352-6362, doi:10.1021/acs.nanolett.9b02497 (2019).

41 Kim, H. G. & Lee, H.-B.-R. Atomic Layer Deposition on 2D Materials. *Chemistry of Materials* **29**, 3809-3826, doi:10.1021/acs.chemmater.6b05103 (2017).

42 Azcatl, A. *et al.* HfO2on UV–O3exposed transition metal dichalcogenides: interfacial reactions study. *2D Materials* **2**, doi:10.1088/2053-1583/2/1/014004 (2015).

43 Walter, T. N., Kwok, F., Simchi, H., Aldosari, H. M. & Mohney, S. E. Oxidation and oxidative vapor-phase etching of few-layer MoS2. *Journal of Vacuum Science & Technology B, Nanotechnology and Microelectronics: Materials, Processing, Measurement, and Phenomena* **35**, doi:10.1116/1.4975144 (2017).

44 Schroder, D. K. Semiconductor Material and Device Characterization. 489-499 (2006).

45 Xu, Y., Minari, T., Tsukagoshi, K., Chroboczek, J. A. & Ghibaudo, G. Direct evaluation of low-field mobility and access resistance in pentacene field-effect transistors. *Journal of Applied Physics* **107**, doi:10.1063/1.3432716 (2010).

Figures

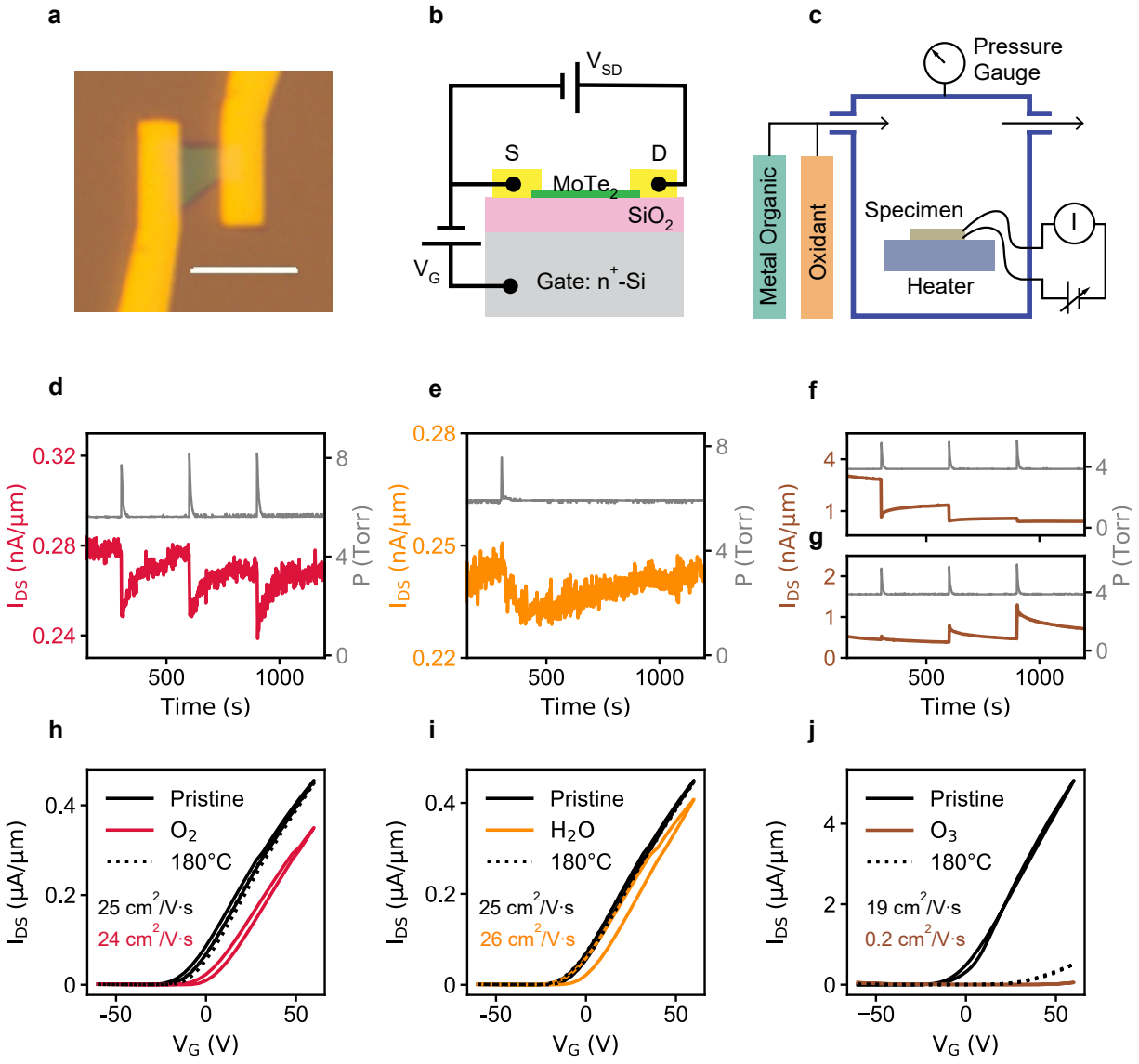

Figure 1. *Operando* measurements of 2D FETs. a, Optical micrograph of a typical $MoTe_2$ FET. The scale bar is 5 μm. **b**, Schematic of a FET connected to three terminals for operation. **c**, Schematic of the modified ALD reactor for *operando* measurements. **d**, **e**, Pulsed oxygen (**d**) and water (**e**) exposures on $MoTe_2$ at 180 °C with V_G set at 0 V and V_{SD} set at 0.05 V, showing reversible changes with time in current density. **f, g**, Pulsed ozone exposures with the same parameters as (**d**, **e**) induce irreversible changes in current density. Ozone pulses in (**g**) directly followed ozone pulses in (**f**). **h**, **i**, Transport characteristics (V_{SD} set at 0.1 V) are reversible with annealing at 180 °C when exposed for 30 min to oxygen (**h**) and water (**i**) at 80 °C. **j**,

Transport characteristics (V_{SD} set at 1 V) are irreversible with annealing when exposed for 5 min to ozone at 80 °C. Pristine and oxidant-exposed mobilities are recorded respectively in (**h**), (**i**), and (**j**).

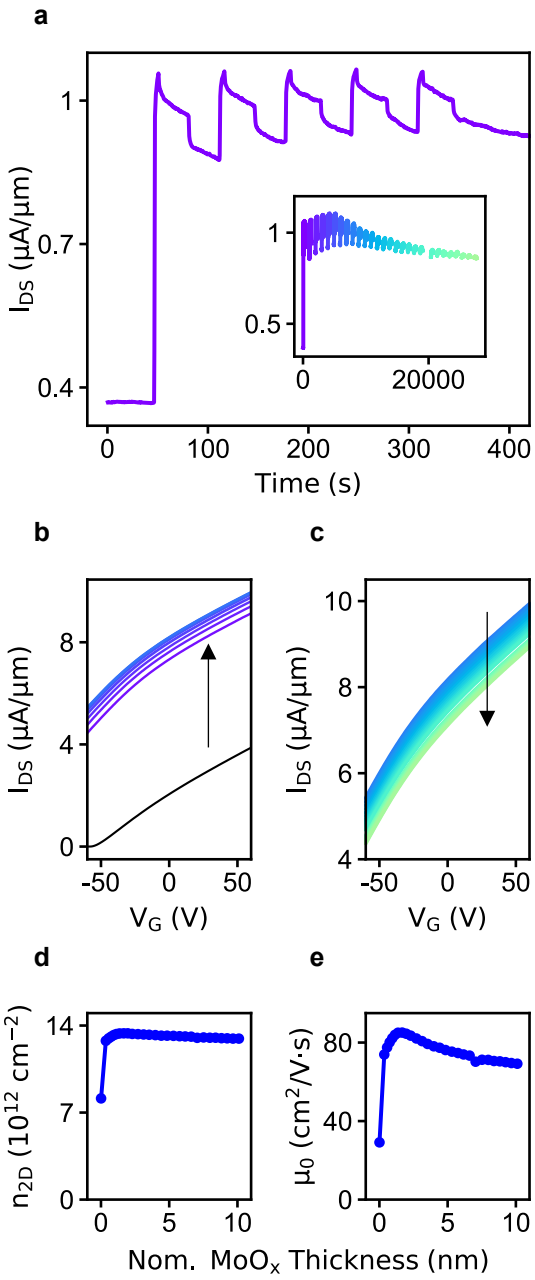

Figure 2. Evolution of electronic properties of MoS_2 during ALD MoO_x growth. a, Current density I_{DS} during the first five cycles of growth. Inset: I_{DS} during the entire growth. **b**, Consecutive transfer curves collected every five ALD cycle for 35 cycles showing increasing current density (indicated by arrow). **c**, Transport characteristics collected for the rest of the growth, during which current density decreases, as indicated by the arrow. **d**, **e**, Carrier concentration n_{2D} (**d**) and intrinsic mobility μ_0 (**e**) are extracted from (**b**) and (**c**), showing significant increase at the beginning of growth.

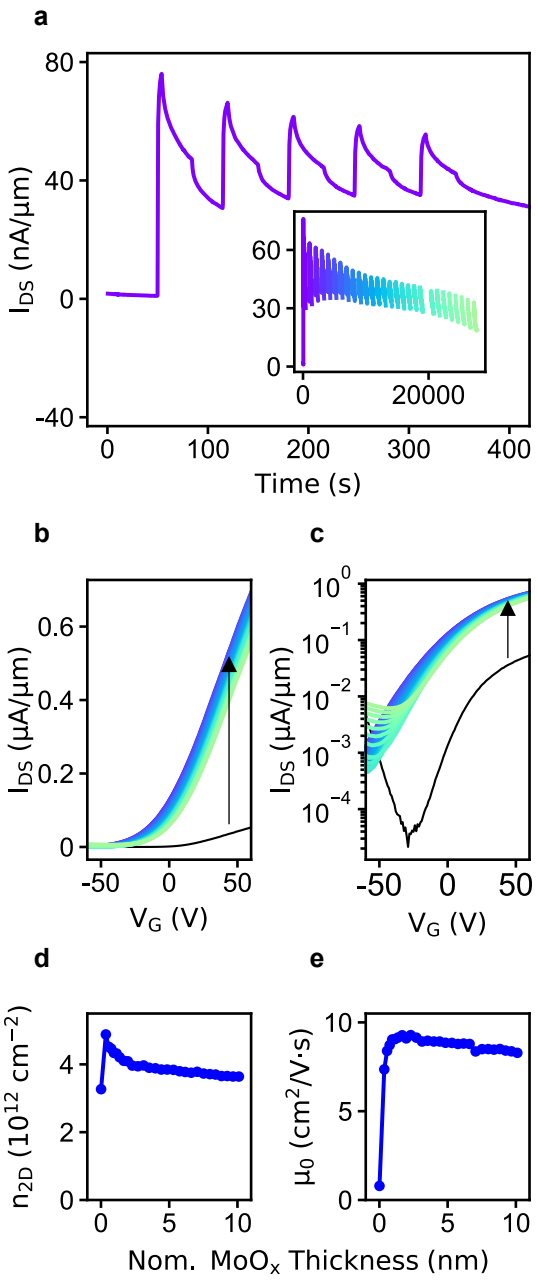

Figure 3. Evolution of electronic properties of $MoTe_2$ during ALD MoO_x growth. a, Current density I_{DS} during the first five cycles of growth. Inset: I_{DS} during the entire growth. **b**, **c,** Consecutive transfer curves collected every five ALD cycles for the entire growth in linear (**b**) and log scale (**c**). The increase in minimum current is partially due to an increase in leakage current (on the order of 10 nA) through MoO_x. Arrows indicate sequence of transfer curves. **d**, **e**, Extracted carrier concentration n_{2D} (**d**) and intrinsic mobility μ_0 (**e**) show significant increases at the beginning of growth.

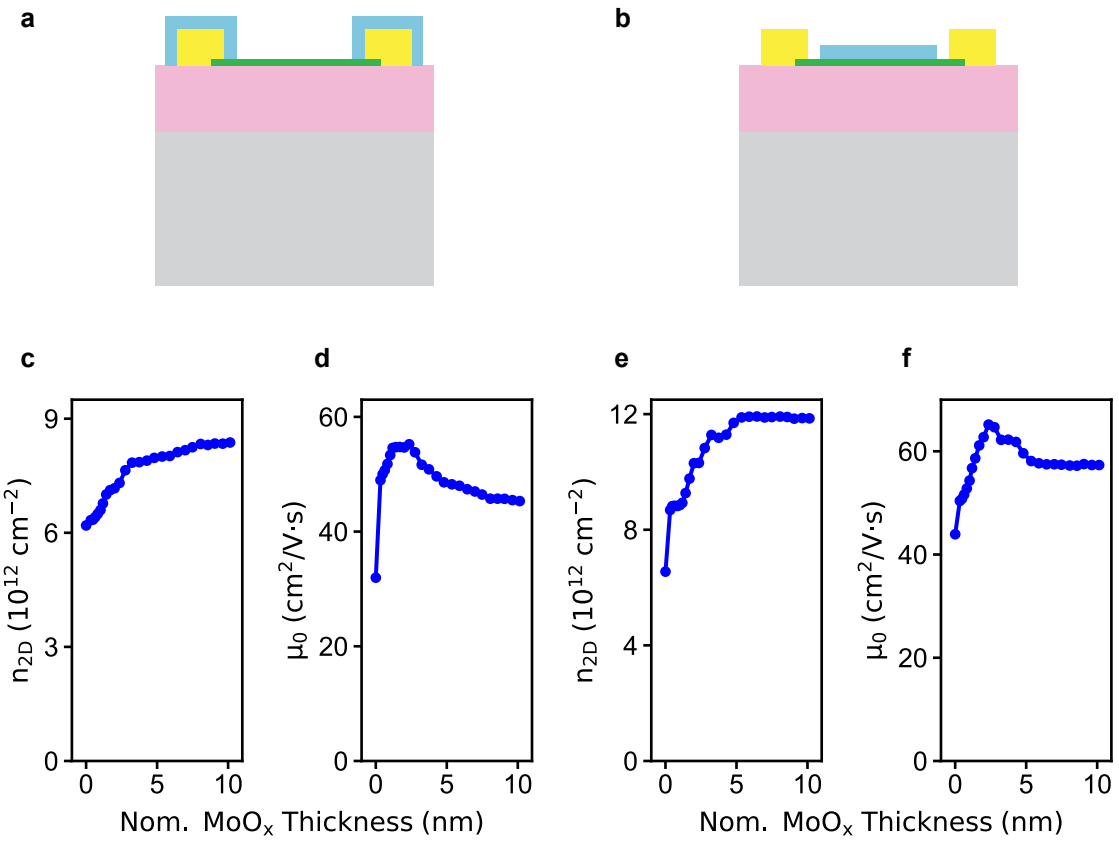

Figure 4. Evolution of n_{2D} and μ_0 of masked MoS_2 FETs during ALD MoO_x growth. a, **b**, Schematics showing Exposed Channel FET (**a**) and Exposed Contacts FET (**b**). **c**, **d**, Extracted n_{2D} (**c**) and μ_0 (**d**) for Exposed Channel FET. **e**, **f**, Extracted n_{2D} (**e**) and μ_0 (**f**) for Exposed Contacts FET.

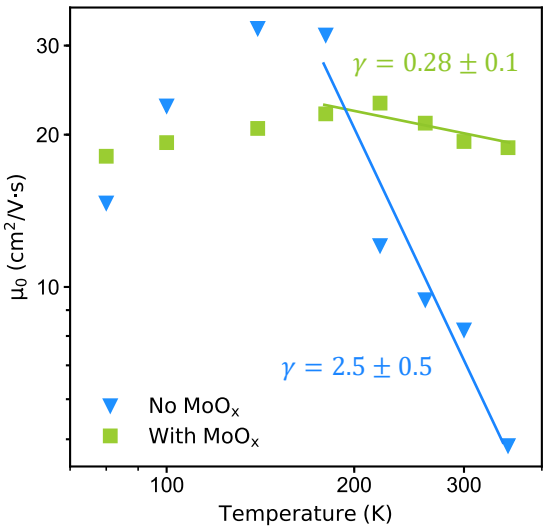

Figure 5. Variation of $MoTe_2$ mobility with temperature before and after MoO_x encapsulation. $\mu \sim T^{\gamma}$ dependence changes from $\gamma = 2.5$ to $\gamma = 0.28$ with MoO_x encapsulation. The error in γ is one standard deviation of the linear fit in the 180-353 K range.

Appendix

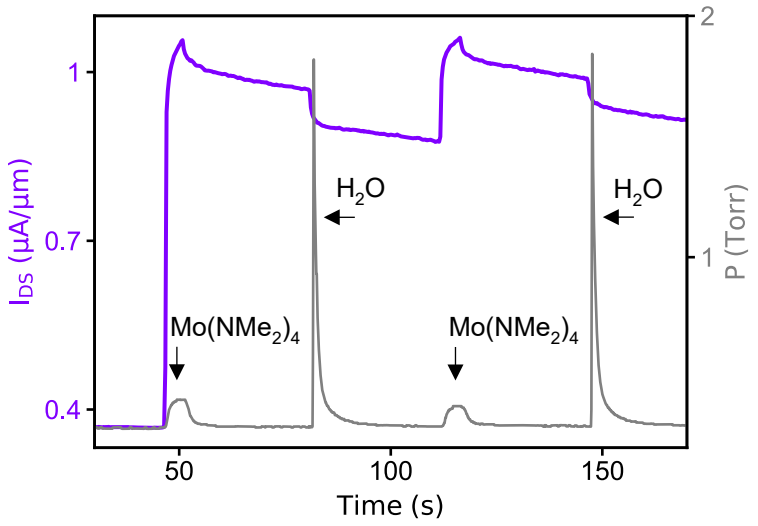

Appendix Figure 1. Time dependence of chamber pressure correlated with I_{DS} of unmasked MoS_2. The first pulse is $Mo(NMe_2)_4$, and the second pulse is H_2O. The two-step cycle alternates until ~ 10 nm of MoO_x is grown.

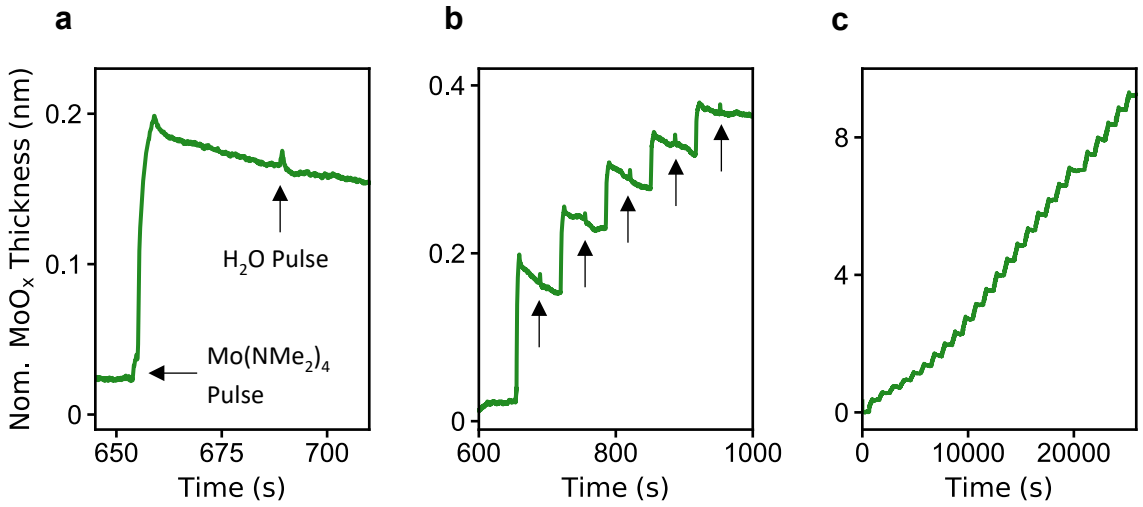

Appendix Figure 2. *In situ* QCM reveals exothermic reaction during ALD growth. a, The first ALD cycle shows when H_2O is pulsed, there is a sharp increase in thickness followed by a decay. **b**, subsequent cycles all demonstrate the same feature shown in (**a**) when H_2O is pulsed (indicated by arrows). **c**, *In situ* QCM monitoring of the entire MoO_x growth.

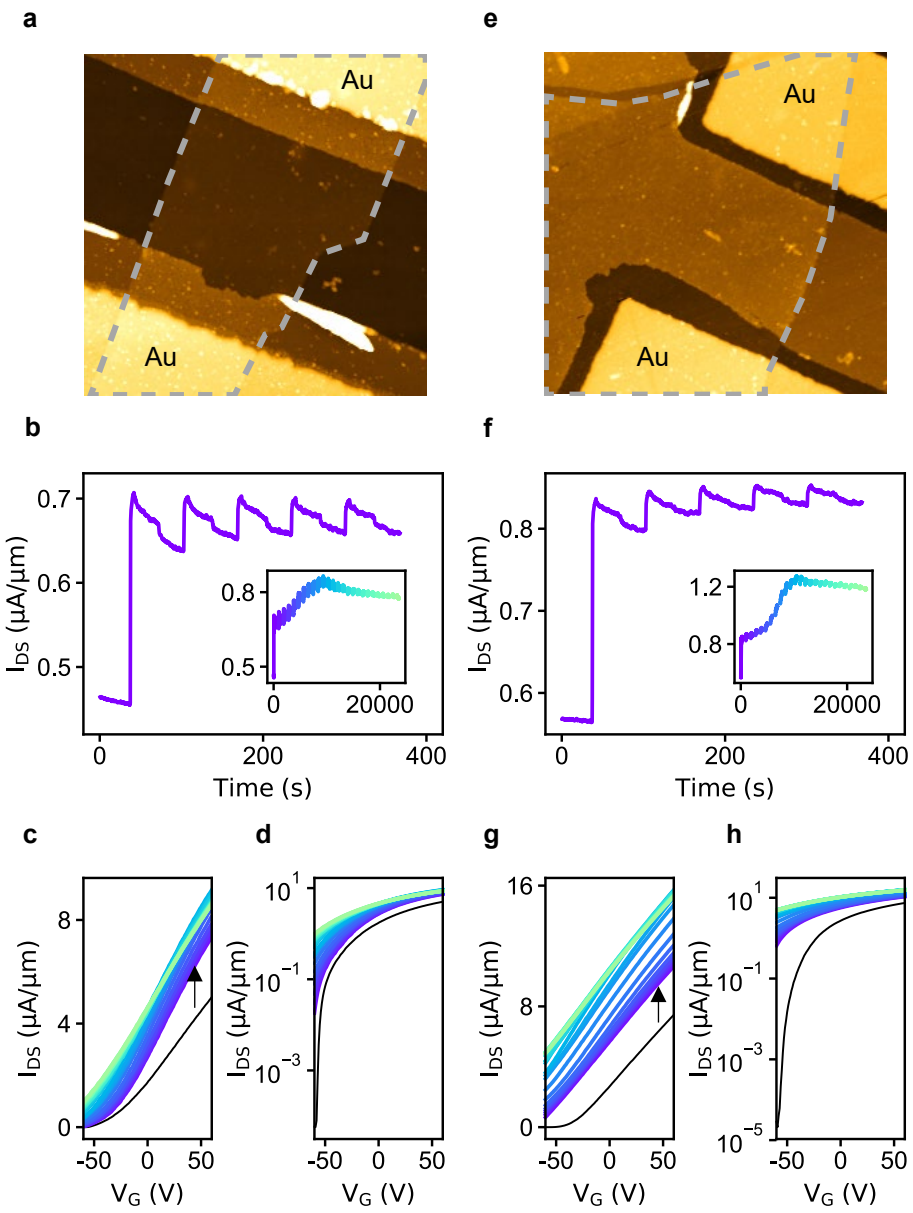

Appendix Figure 3. Evolution of electronic properties of Masked MoS_2 FETs during ALD MoO_x growth. a, AFM scan of Exposed Channel FET. The dashed line traces the MoS_2 flake. **b-d**, *Operando* measurements of Exposed Channel FET during growth. (**b**) shows I_{DS} during the first five cycles of growth. Inset: I_{DS} during the entire growth. Transport characteristic collected every five ALD cycle are shown in linear (**c**) and log (**d**) scale. Arrow indicate sequence of transfer curves. **e**, AFM scan of Exposed Contacts FET. The dashed line traces the MoS_2 flake. **f-h**, *Operando* measurements of Exposed Contacts FET during growth. (**f**) shows I_{DS} during the first five cycles of growth. Inset: I_{DS} during the entire growth. Transport characteristic collected every five ALD cycles are shown in linear (**g**) and log (**h**) scale. Arrows indicate the sequence of transfer curves.

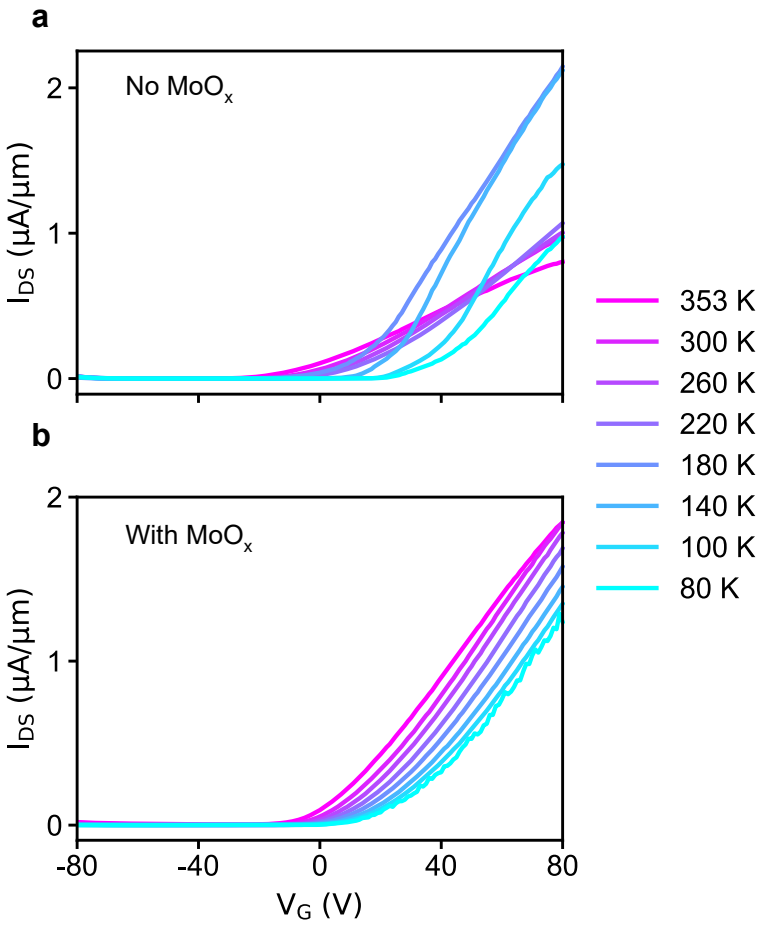

Appendix Figure 4. Transport characteristics of $MoTe_2$ FET at variable temperatures pre- (a) and post- (b) ALD MoO_x growth.

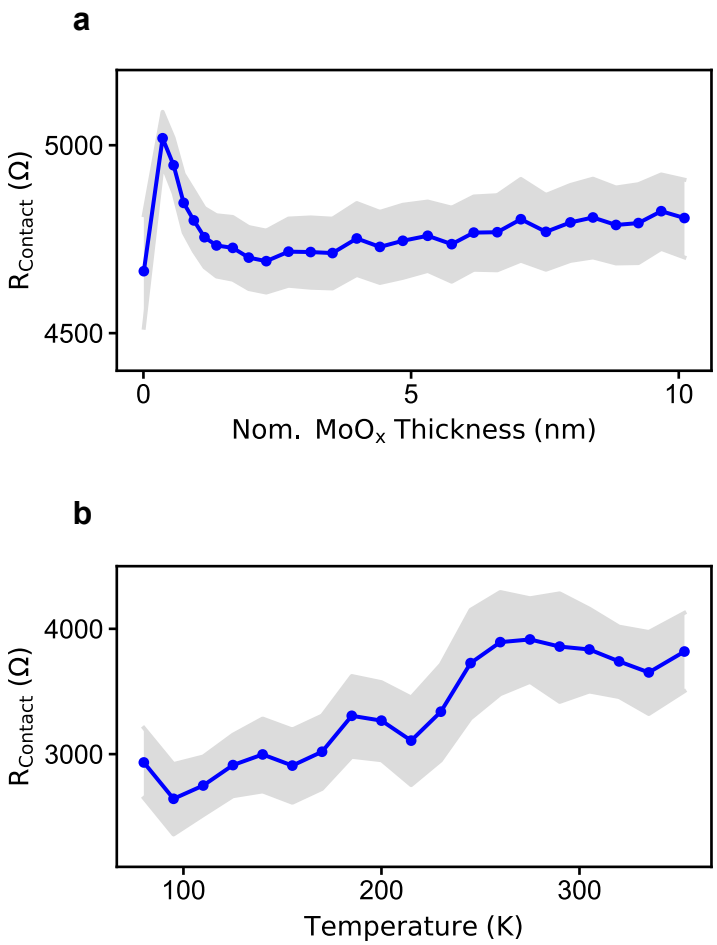

Appendix Figure 5. Variations in contact resistance. a, *Operando* contact resistance during MoO_x growth on unmasked MoS_2. Grey regions indicate three standard deviations for each extracted contact resistance. Due to the small variation in contact resistance throughout the growth, it is assumed constant for n_{2D} and μ_0 extraction. **b**, Contact resistance for unmasked MoS_2 from 80 K to 353 K. Grey regions indicate three standard deviations for each extracted contact resistance. Due to the small variation in contact resistance with respect to temperature, it is assumed constant in μ_0 extraction.

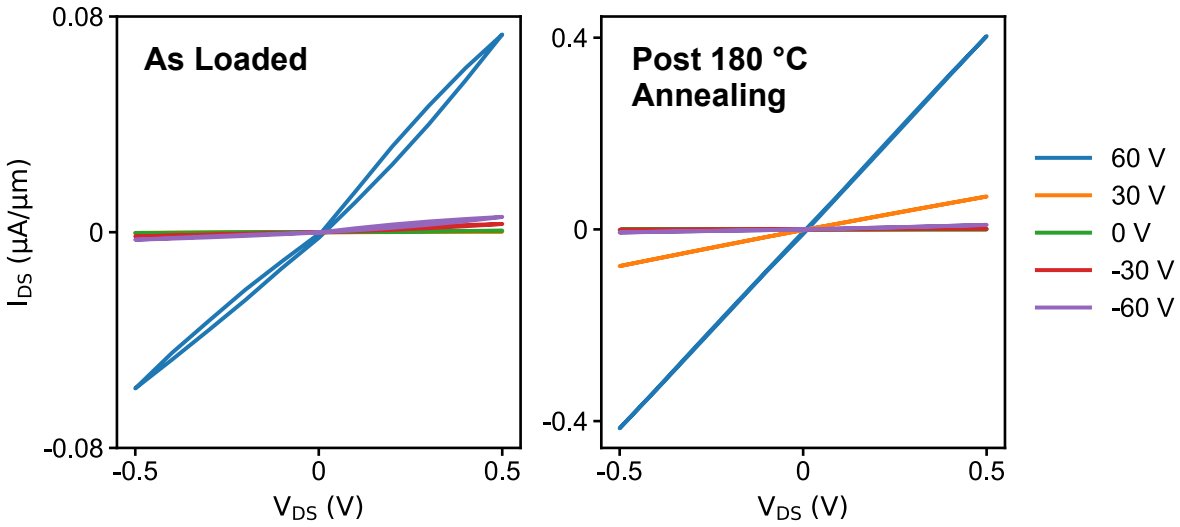

Appendix Figure 6. Output curves of $MoTe_2$ as loaded into the ALD chamber and post 180 °C annealing.

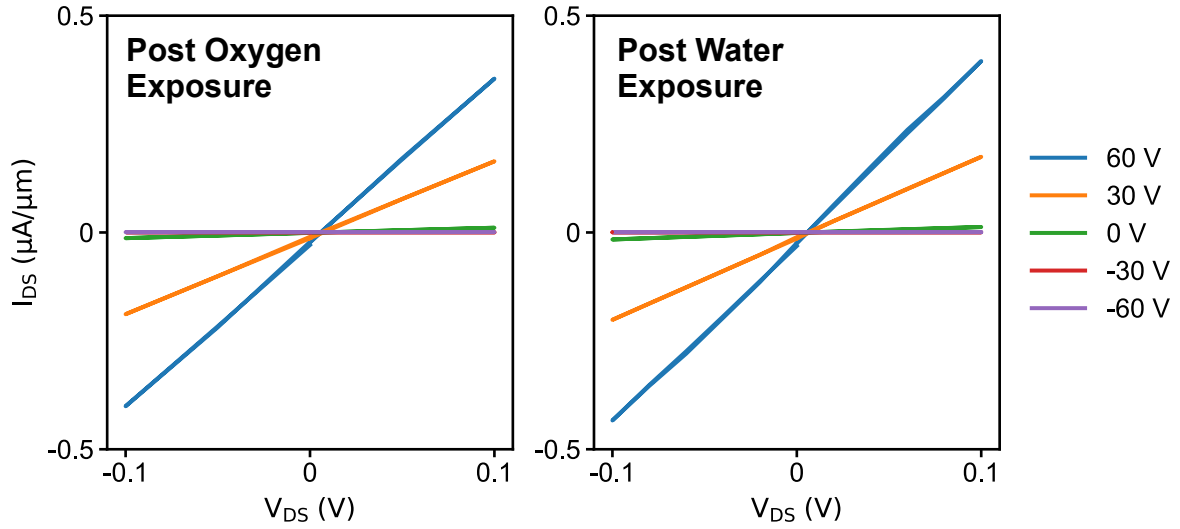

Appendix Figure 7. Output curves of $MoTe_2$ post oxygen and water exposure.

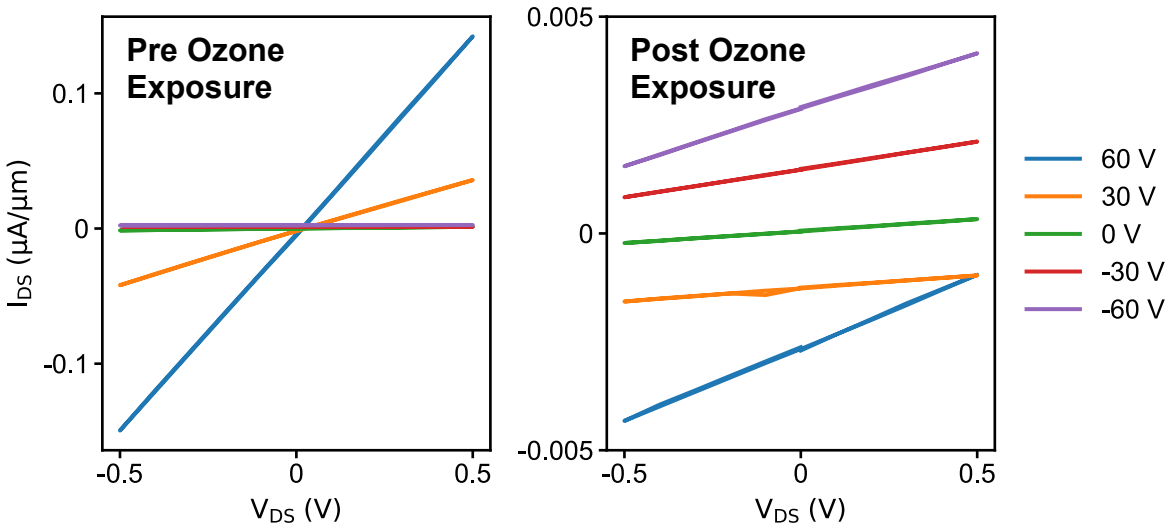

Appendix Figure 8. Output curves of $MoTe_2$ pre and post ozone exposure. With ozone exposure, leakage current increased, likely due to oxidation of $MoTe_2$ surface.

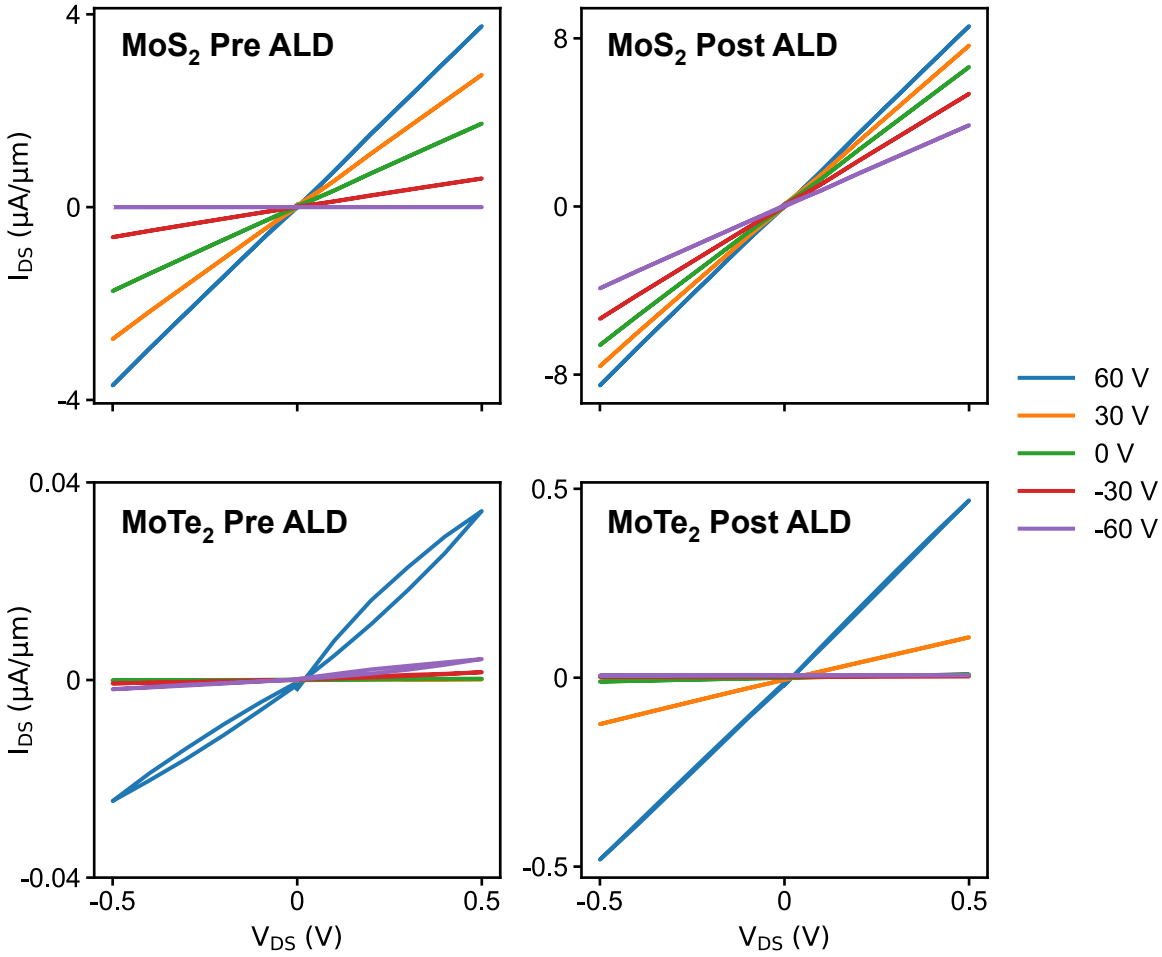

Appendix Figure 9. Output curves of MoS_2 and $MoTe_2$ pre and post ALD MoO_x/Al_2O_3 growth.

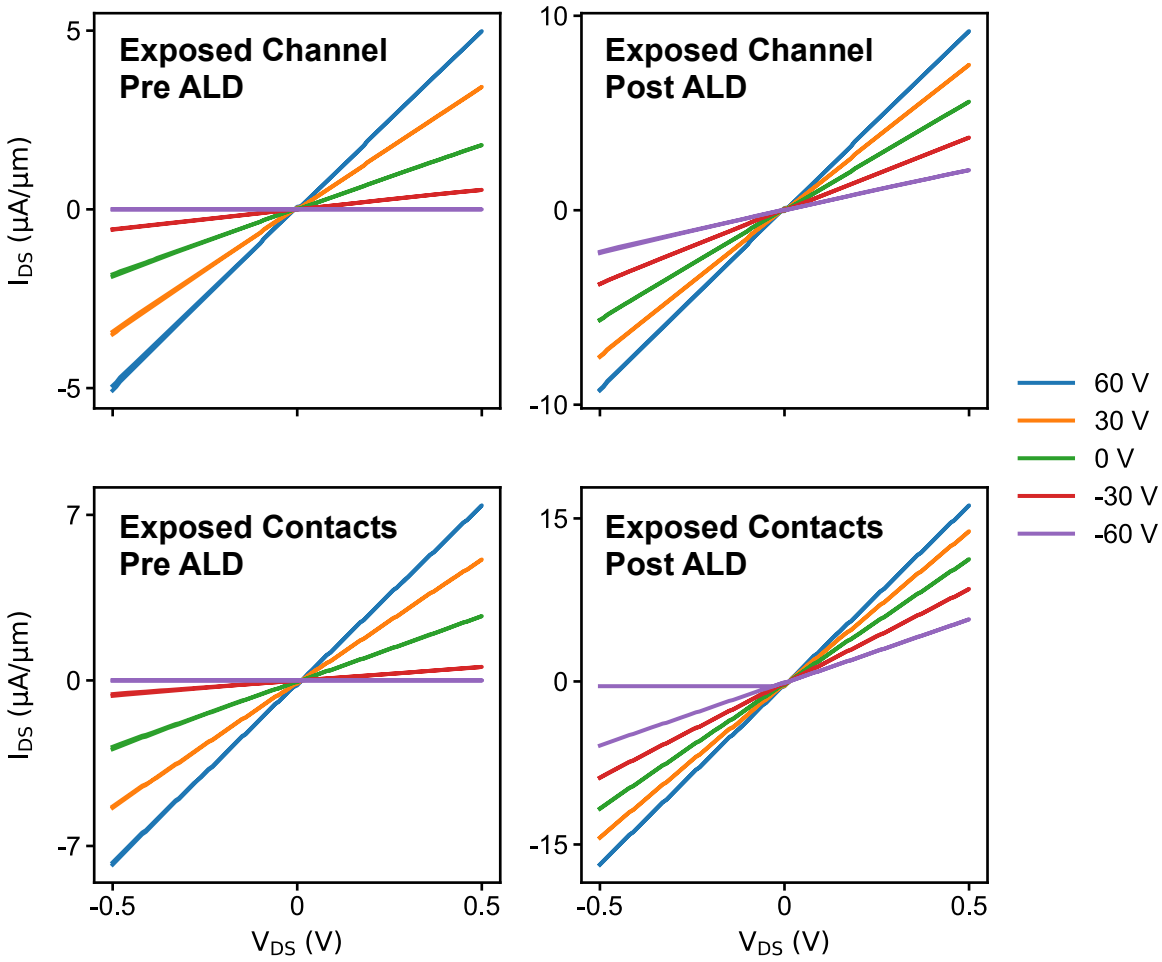

Appendix Figure 10. Output curves of Exposed Channel and Exposed Contacts MoS_2 pre and post ALD MoO_x/Al_2O_3 growth.

Appendix Table 1. Table of values for percent increase calculation for unmasked MoS_2 FET.

	ALD Cycle 0	**ALD Cycle 1**	**ALD Cycle 5**	**% Inc**
n_{2D}	8.1×10^{12} cm^{-2}	--	1.3×10^{13} cm^{-2}	60
μ_0	29 cm^2/V·s	--	74 cm^2/V·s	160
I_{DS}	0.37 μA/μm (forward sweep*) 0.37 μA/μm (backward sweep)	0.88 μA/μm	0.92 μA/μm	140$^{\perp}$ 140$^{\perp}$

* I_{DS} forward sweep comes from transfer curve measurement; backward sweep comes from I_{DS} real-time monitoring. Applies to Appendix Table 1-2. Appendix Table 3-4 only reports I_{DS} from real-time monitoring.

$^{\perp}$ % increase calculated between ALD Cycle 0 and ALD Cycle 1. ALD Cycle 5 I_{DS} is reported, but not used in calculations. Applies to Appendix Table 1-4.

Appendix Table 2. Table of values for percent increase calculation for unmasked $MoTe_2$ FET.

	ALD Cycle 0	**ALD Cycle 1**	**ALD Cycle 5**	**% Inc**
n_{2D}	3.3×10^{12} cm^{-2}	--	4.9×10^{12} cm^{-2}	50
μ_0	0.79 cm^2/V·s	--	7.4 cm^2/V·s	840
I_{DS}	4.7 nA/μm (forward sweep) 1.4 nA/μm (backward sweep)	31 nA/μm	30 nA/μm	560 2100

Appendix Table 3. Table of values for percent increase calculation for Exposed Channel MoS_2 FET.

	ALD Cycle 0	**ALD Cycle 1**	**ALD Cycle 5**	**% Inc**
n_{2D}	6.2×10^{12} cm^{-2}	--	6.3×10^{12} cm^{-2}	0
μ_0	32 cm^2/V·s	--	49 cm^2/V·s	50
I_{DS}	27 μA/μm	38 μA/μm	40 μA/μm	40

Appendix Table 4. Table of values for percent increase calculation for Exposed Contacts MoS_2 FET.

	ALD Cycle 0	**ALD Cycle 1**	**ALD Cycle 5**	**% Inc**
n_{2D}	6.6×10^{12} cm^{-2}	--	8.7×10^{12} cm^{-2}	30
μ_0	44 cm^2/V·s	--	50 cm^2/V·s	10
I_{DS}	34 μA/μm	48 μA/μm	50 μA/μm	40

Appendix Table 5. Table of Devices.

Device #	Channel Material	Length (μm)	Width (μm)	Thickness (nm)	Figure #	Measurement/Experiment
Te18_Dev2	$MoTe_2$	4.0	2.7	8	Figure 1de, Appendix Figure 6	Oxygen and water exposure real-time monitoring
Te12_Dev2	$MoTe_2$	5.0	2.5	9	Figure 1fg, Appendix Figure 8	Ozone exposure real-time monitoring
Te11_Dev1	$MoTe_2$	3.9	3.5	5	Figure 1hi, Appendix Figure 7	Oxygen and water exposure transfer curve measurements
Te18_Dev1	$MoTe_2$	2.0	2.5	8	Figure 1j	Ozone exposure transfer curve measurements
S-Te1_Dev1	MoS_2	4.0	6.1	7[#]	Figure 2, Appendix Figures 1, 2, 5a, 9	MoO_x ALD Growth 1 MoS_2 Experiment
Te12_Dev1	$MoTe_2$	4.3	2.2	7	Figure 3, Appendix Figures 2, 9	MoO_x ALD Growth 1 $MoTe_2$ Experiment
S4_Dev1	MoS_2	3.0	2.0	5	Figure 4cd, Appendix Figures 3abcd, 10	MoO_x ALD Growth 2 Exposed Channel Experiment
S5_Dev2	MoS_2	3.0	2.4	5	Figure 4ef, Appendix Figures 3efgh, 10	MoO_x ALD Growth 2 Exposed Contacts Experiment
Te42_Dev2	$MoTe_2$	3.0	2.2	8	Figure 5, Appendix Figure 4	MoO_x ALD Growth 3 variable temperature transfer curve measurements
Te35-MoS2_Dev2	MoS_2	3.0	4.0	8[#]	Appendix Figure 5b	Variable temperature transfer curve measurements

[#] Thicknesses estimated from S-Te1_Dev2, with a thickness of 6 nm.